Simulation of laser propagation through a three-layer human skin model in the spectral range from 1000 to 1900 nm

Babak Nasouri
Thomas E. Murphy
Halil Berberoglu

Simulation of laser propagation through a three-layer human skin model in the spectral range from 1000 to 1900 nm

Babak Nasouri, Thomas E. Murphy, and Halil Berberoglu[*]
The University of Texas at Austin, Mechanical Engineering Department, 204 E. Dean Keeton Street, Austin, Texas 78712

Abstract. For understanding the mechanisms of low-level laser/light therapy (LLLT), accurate knowledge of light interaction with tissue is necessary. We present a three-dimensional, multilayer reduced-variance Monte Carlo simulation tool for studying light penetration and absorption in human skin. Local profiles of light penetration and volumetric absorption were calculated for uniform as well as Gaussian profile beams with different spreads over the spectral range from 1000 to 1900 nm. The results showed that lasers within this wavelength range could be used to effectively and safely deliver energy to specific skin layers as well as achieve large penetration depths for treating deep tissues, without causing skin damage. In addition, by changing the beam profile from uniform to Gaussian, the local volumetric dosage could increase as much as three times for otherwise similar lasers. We expect that this tool along with the results presented will aid researchers in selecting wavelength and laser power in LLLT. © *2014 Society of Photo-Optical Instrumentation Engineers (SPIE)* [DOI: 10.1117/1.JBO.19.7.075003]

Keywords: low-level laser therapy; Monte Carlo method; laser penetration; absorption; human tissue; skin damage threshold.

Paper 140173PRR received Mar. 15, 2014; revised manuscript received Jun. 3, 2014; accepted for publication Jun. 5, 2014; published online Jul. 7, 2014.

1 Introduction

As an effective method for improving tissue repair, pain reduction, and hair growth, low-level laser therapy (LLLT) has recently become a progressively dominant therapy. In this method, lasers with low power ranges from 10^0 to 10^3 mW and wide spectral ranges from 300 to 10,600 nm are used.[1] The success of LLLT in expediting the healing rate of skin wounds has been vastly reported in the literature for both human and animal cases.[1–9] Fillipin et al.[2] and Rizzi et al.[3] reported that using a 904-nm gallium arsenide (Ga-As) laser light-emitting diode with an average power of 45 mW considerably reduced the oxygen release and inflammatory responses of muscle tissue following a trauma. Moreover, Hopkins et al.[4] showed that LLLT enhanced the healing speed of human forearm abrasions using laser diodes with wavelengths from 660 to 940 nm at powers from 15 to 25 mW. Similarly, a noticeable increase in skin cell growth rate in both pigs[6] and humans[7] has been observed following LLLT.

Despite these successful cases, the effectiveness of LLLT was not clear in other cases. For example, although da Rosa et al.[10] reported a considerable enhancement in the healing process of osteoarthritis using an 808-nm As-Ga-Al laser (100 mW, 3.57 W/cm^2, 40 s), Taradaj et al.[11] claimed that using an 810-nm As-Ga-Al laser (4 J/cm^2, 65 mW) did not improve the healing of venous leg ulcers. These contradictions indicate that using LLLT in a "shot in the dark" manner cannot make this method a reliable therapy method. In order to have a successful therapy, laser power should be effectively delivered to the target layer without any considerable absorption in other layers.[3–5] Depending upon the therapy, this target layer can be the dermis, the subcutaneous, or the muscle layer beneath the skin.

Moreover, the dependence of laser power absorption and penetration depths on the input parameters, such as the wavelength, the power, and the beam profile, should be investigated more precisely to improve the understanding of laser–tissue interaction. As an approach to resolve these issues, laser penetration through tissues was studied numerically mostly using a single-layer model for the human skin.[12–20] For example, Roeva et al.[18] investigated the laser penetration by applying LLLT on 142 patients and also evaluating light delivery within the tissue using the Monte Carlo method. They simulated human tissue as a single-layer medium with constant optical properties and showed the effect of absorption and scattering coefficients on laser penetration in the skin. Moreover, Stoykova and Sabotinov[19] considered a single-layer model for periodontal tissue and investigated the influences of tissue optical properties (anisotropy factor, tissue refraction index, etc.) on energy deposition within the medium. In another case, Parvin et al.[20] focused on the energy distribution in the dermis using Monte Carlo simulation and studied the effect of nonisotropic scattering on the density of absorbed photons. Most previous studies on LLLT considered the spectral range from 600 to 1000 nm due to the high penetration depths associated and the availability of inexpensive laser diodes within this spectral range.

In recent years, there have been significant advancements in near-infrared (NIR) laser technology, making inexpensive lasers in the spectral range from 1000 to 1900 nm available. In addition, this underutilized wavelength range can provide advantages over the more conventional range, coupling energy more effectively to the tissue for therapeutic applications. However, achieving large enough penetration depths can be challenging and wavelength selection can significantly affect the location of treatment and the dosage of radiative energy deposited. Due to this sensitivity of LLLT, it has been difficult

*Address all correspondence to: Halil Berberoglu, E-mail: berberoglu@mail .utexas.edu

to understand the mechanisms of this method. This study, for the first time, presents a precise analysis of spectral dosimetry for LLLT using a low-variance Monte Carlo method, and taking into account the beam profile of the source laser. We modeled human skin as a multilayer medium with variable optical properties and implemented a three-dimensional (3-D) low-variance Monte Carlo method to simulate laser penetration in the wavelength range from 1000 to 1900 nm. Moreover, we investigated the skin damage threshold in this wavelength range and reported the maximum permitted exposure duration based on ANSI standards.

2 Analysis

In this study, human skin was modeled as a three-layer rectangular cuboid with the specific geometry as given in Fig. 1. The thicknesses of epidermis, dermis, and subcutaneous layers were 0.3, 1.2, and 3.0 mm, respectively.[21] A collimated laser beam was incident normally on the top surface of the skin (epidermis). The laser beam diameter was obtained from the characteristics of the VetLase Inc.™ laser probe and considered to be 6.1 mm.

In order to make the problem mathematically tractable, the following assumptions were made: (1) refractive index and anisotropy factors were constant within each layer, (2) surrounding air had a refractive index of 1.00 and was nonparticipating, (3) due to high absorptivity of the muscle layer beneath the subcutaneous layer,[22,23] this layer was assumed to absorb light completely, and (4) the blackbody emission by the skin and the surrounding tissues within the wavelength range of interest was negligible at the normal body temperature of 36°C.

2.1 Governing Equations and Boundary Conditions

Transport of laser radiation within skin can be described by the radiative transport equation (RTE). The 3-D steady-state RTE (Ref. 24) can be written as

$$\frac{dI_\lambda(S, \Omega)}{dS} = -\mu_a I_\lambda(S, \Omega) - \mu_s I_\lambda(S, \Omega)$$
$$+ \frac{\mu_s}{4\pi} \int_{4\pi} I_\lambda(S, \Omega_i) \Phi_\lambda(\Omega_i, \Omega) d\Omega_i, \quad (1)$$

where S is the path length, $I_\lambda(S, \Omega)$ is the local radiation intensity, and μ_a and μ_s are the absorption and scattering coefficients of skin, respectively. Moreover, $\Phi_\lambda(\Omega_i, \Omega)$ is the scattering phase function which describes the probability of redirecting the incoming intensity from an arbitrary direction Ω_i to the direction of interest Ω. In this study, the scattering phase function is approximated with the Henyey-Greenstein function[24] as
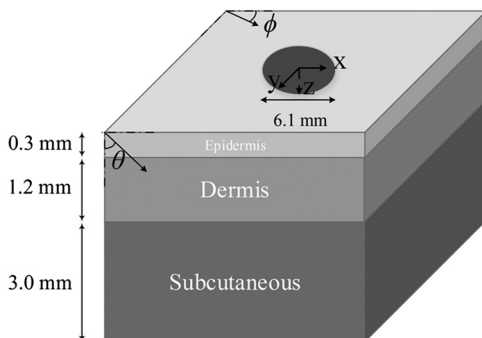

Fig. 1 The schematic view of three-layer skin model.

$$\Phi_{HG}(\Omega) = \frac{1 - g^2}{[1 + g^2 - 2g\cos(\Omega)]^{3/2}}, \quad (2)$$

where g, known as the anisotropy factor, is the mean cosine of scattering angle Θ and is related to the phase function by

$$g = \overline{\cos(\Theta)} = \frac{1}{4\pi} \int_{4\pi} \Phi(\Theta)\cos(\Theta)d\Omega_i. \quad (3)$$

Anisotropy factor approaches $+1$ for strongly forward scattering media, 0 for isotropic scattering, and -1 for strongly backward scattering media. In this study, the anisotropy factor and the refractive index of each layer has been considered individually and are obtained from the literature[25,26] over the spectral range from 1000 to 1900 nm. The anisotropy factors considered for the epidermis, the dermis, and the subcutaneous layers were 0.80, 0.91, and 0.75, and the obtained refractive indexes for these layers were reported as 1.34, 1.40, and 1.44, respectively.

At the top boundary, reflectance was taken into account through the Fresnel equation according to[24]

$$\rho_\lambda = \frac{1}{2} \left[\left(\frac{n_{\lambda,1}\cos\theta_2 - n_{\lambda,2}\cos\theta_1}{n_{\lambda,1}\cos\theta_2 + n_{\lambda,2}\cos\theta_1} \right)^2 \right.$$
$$\left. + \left(\frac{n_{\lambda,1}\cos\theta_1 - n_{\lambda,2}\cos\theta_2}{n_{\lambda,1}\cos\theta_1 + n_{\lambda,2}\cos\theta_2} \right)^2 \right], \quad (4)$$

where θ_1 and $n_{\lambda,1}$ are the angle and the refractive index of the incident side and θ_2 and $n_{\lambda,2}$ are those for the transmitted side. Here, the refraction was accounted for by Snell's law[24] as

$$n_{\lambda,1}\sin\theta_1 = n_{\lambda,2}\sin\theta_2. \quad (5)$$

Finally, in the case of collimated radiation, the boundary conditions for the top surface can be written as

$$I_\lambda(x, y, z = 0) = G_{\lambda,0}\delta(\theta_c) \quad (6)$$

and that for the bottom surface as

$$I_\lambda(x, y, z = l, \pi/2 < \theta < \pi, \phi) = 0, \quad (7)$$

where l is the thickness of the skin and $G_{\lambda,0}$ is the incident laser irradiance, which can be calculated based on the laser power used.

2.2 Closure Laws

The optical properties of human skin have been widely reported in the literature.[25–30] However, since several factors (e.g., age, color, etc.) can considerably affect these optical properties, the reported values vary significantly. These large variations in skin optical properties are expected to cause variations in the results obtained through simulations. In this study, we chose to use the radiation characteristics of the skin layers reported by Simpson et al.,[23] Troy and Thennadil,[25] and Iino et al.[27] as (1) these values have been widely used by other researchers simulating light transport[31–34] and (2) these were some of the only credible sources found in the literature reporting values for three-layer skin model. The values of absorption and scattering coefficients used in this study are shown in Table 1.

Table 1 Absorption and scattering coefficients of skin layers at wavelengths of 1150, 1350, 1550, 1650, and 1780 nm.

Wavelength	Skin layer	Absorption coefficient— μ_a (cm^{-1})	Scattering coefficient— μ_a (cm^{-1})
$\lambda = 1150$ nm	Epidermis	0.1	146.8
	Dermis	1.1	146.8
	Subcutaneous	0.6	100.5
$\lambda = 1350$ nm	Epidermis	0.4	142.1
	Dermis	2.8	142.1
	Subcutaneous	0.3	95.8
$\lambda = 1550$ nm	Epidermis	1.0	137.9
	Dermis	7.7	137.9
	Subcutaneous	0.9	91.5
$\lambda = 1650$ nm	Epidermis	1.0	135.9
	Dermis	4.5	135.9
	Subcutaneous	0.8	89.2
$\lambda = 1780$ nm	Epidermis	1.5	132.9
	Dermis	6.4	132.9
	Subcutaneous	6.4	85.9

Then, we used a nondimensional parameter, namely transport optical thickness, to select the wavelengths of interest. Transport optical thickness indicates the overall strength of the medium in attenuating radiation at a given wavelength in the penetration direction. It can be written as

$$\tau_\lambda = \sum_{i=1}^{n} d_i \mu_{a,i} + \sum_{i=1}^{n} (1 - g_i) d_i \mu_{s,i}, \qquad (8)$$

where d_i is the physical thickness, g is the anisotropy factor, and $\mu_{a,i}$ and $\mu_{s,i}$ are absorption and scattering coefficients of the i'th layer, respectively. Figure 2 illustrates this parameter for the
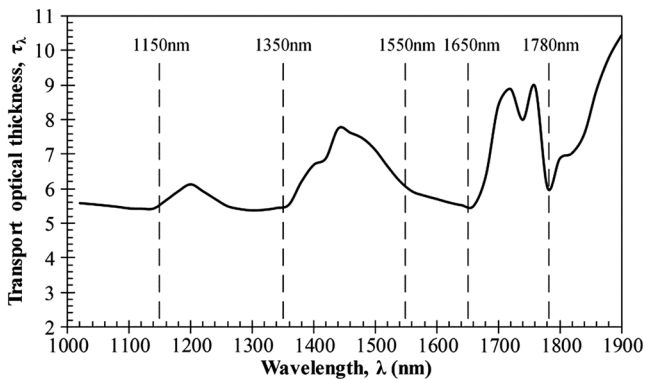

Fig. 2 Transport optical thickness of human skin for wavelengths between 1000 and 1900 nm. Dashed lines indicate wavelengths with relatively low transport optical thicknesses.

wavelengths between 1000 and 1900 nm. For most LLLT applications, deep laser light penetration is desired. In most common lower-wavelength ranges (up to ~1000 nm), penetration is not an issue and a laser can effectively penetrate through the tissue. However, for the wavelength range considered in this study, deep penetration is not trivial and is reserved for certain wavelengths dictated by a combination of absorption and scattering phenomena. As we have shown, the penetration depth correlates well with the transport optical thickness. Thus, we considered wavelengths that are corresponded to relatively low transport optical thicknesses, as indicated, for demonstrating the large penetration depths possible within this wavelength range.

2.3 Method of Solution

In this study, a 3-D multilayer reduced-variance Monte Carlo method was implemented and validated against benchmark solutions. The Monte Carlo technique was first proposed by Metropolis and Ulam[35] as a statistical approach for studying differential equations. More recently, Prahl et al.[17] applied the variance reduction technique, proposed by Kahn and Harris,[36] to the Monte Carlo method and implemented a reduced-variance Monte Carlo for simulating light propagation in tissue. By using the variable step-size walking process in this method, the high variance in the normal Monte Carlo method can be resolved without a considerable CPU time increase. To illustrate, light is modeled as a large number of energy packets. The total energy is then distributed uniformly over these packets; thus, each packet carries an equal amount of energy. The method tracks each energy packet as it is absorbed, scattered, backscattered, transmitted, or reflected within the skin. For the packets that scatter within the skin, a fraction of their energy will be absorbed and deducted in each interaction as

$$W = \frac{\mu_a}{\mu_a + \mu_s} W_0, \qquad (9)$$

where W_0 is the packet's initial energy and W is the packet's energy after the interaction. Based on this method, a packet can propagate infinitely and its energy will never reach zero. Thus, an energy threshold is defined to terminate the packet with an energy level below the minimum. By minimizing this energy threshold, the accuracy of the results can be improved. We observed that by decreasing this energy threshold from $0.001 \times W_0$ to $0.0001 \times W_0$, results changed ~0.01%, while the CPU time increased by ~1 h. Therefore, the value of $0.001 \times W_0$ was considered as the threshold energy. In order to track late-stage propagation, such a weakened packet is considered for survival at the m'th stage (i.e., the stage where its energy falls below threshold) using a roulette technique.[17] According to this technique, if a packet's energy falls below the threshold value at m'th stage of propagation, the packet's energy is either increased to $m \times W$ or it is eliminated using a random process. The eliminated packets are monitored to satisfy the energy conservation. Then, based on the location of the absorbed packets, the amount of absorbed power can be calculated. Figure 3 shows the flow chart for this multilayer 3-D reduced-variance Monte Carlo scheme used in this study. This Monte Carlo method was implemented on a hyperthreading 3.33 GHz Xeon processor with 24 GB of shared memory. The averaged CPU time for each simulation was ~20 min.
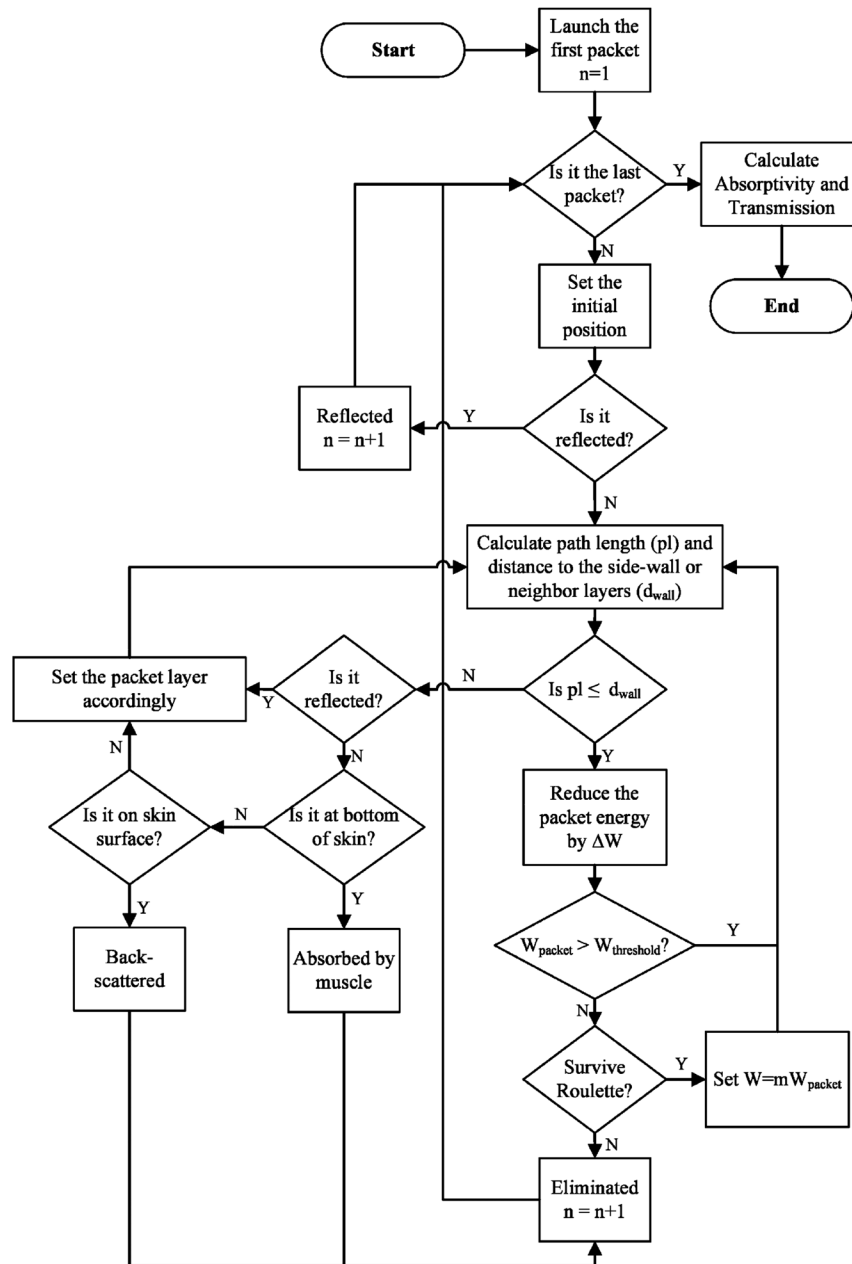
Fig. 3 The flow chart of solution algorithm used in this study for the multilayer three-dimensional reduced-variance Monte Carlo scheme. Light is modeled as large number of packets, and each packet is tracked until it gets absorbed, transmitted, or reflected.

This code was validated for both scattering and nonscattering media cases. In the nonscattering case, a rectangular cuboid of water has been considered as a purely absorbing medium. Transmissivity of the cuboid layer was obtained from the Monte Carlo method as well as Beer-Lambert's law,[24] using Wieliczka et al's[37] data for water optical properties. In case of an anisotropic media, a medium with an optical thickness of 2.0, an albedo of 0.9, and anisotropy factor of 0.75 was simulated and the obtained results were compared to those of Van de Hulst[38] and Prahl et al.[17] Based on these comparisons, the percent deviations for the transmittance with respect to the Beer-Lambert law, Van de Hulst's tables, and Prahl et al. were 0.01, 0.11, and 0.30%, respectively. Besides these benchmark solutions, the presented results of the implemented method

can be experimentally verified by using multilayered tissue phantoms of known optical properties.

Moreover, sensitivity of the Monte Carlo code on the number of energy bundles used was analyzed to ensure that the obtained results were independent of this choice. By increasing the number of packets from 10^6 to 10^7, changes in the absorptance results were <0.1%, but the CPU time increased by 20 h. Thus, 10^6 energy bundles with a total power of 155 mW were used in all of the results reported in this paper.

3 Results and Discussion

First, we performed the reduced-variance Mote Carlo simulations at the selected wavelengths and studied the penetration and absorption of lasers with uniform profiles in different

skin layers. Then, we processed our results in the perspective of power delivery and compared the selected wavelengths based on this factor. Finally, we reported the maximum allowable exposure time for the considered laser probe based on the maximum absorbed dosage and available standards.

3.1 Propagation and Absorption of NIR Radiation in Skin Layers

The relevant parameter in laser treatment of tissues is the dosage, i.e., the amount of energy absorbed at a given volume. Local variations of dosage can significantly affect a treatment and can be defined as

$$D_v = P_{abs} \cdot t_{exp}, \tag{10}$$

where P_{abs} is the volumetric absorbed power density (mW/mm^3) and t_{exp} is the exposure duration. Thus, here we reported our results based on the density of absorbed power,

which provides the flexibility of calculating the dosage at different exposure times.

For illustrative purposes, we used the laser characteristics of the VetLase Inc.™ laser probe in our simulation. Thus, we considered a collimated laser beam of diameter 6.1 mm with an irradiance of 155 mW at the selected wavelengths. The local absorbed power density was measured by using results of the implemented Monte Carlo code. To do so, for a given volume the fraction of absorbed packets were counted and multiplied by the amount of energy that each packet carries. Hence, by dividing the measured absorbed energy by its corresponding volume, the local absorbed power was measured. Figure 4 shows the volumetric power density as a function of location within the three-layer skin model on the $x - z$ plane. In order to generate this map, the 3-D results of absorbed power within the skin were integrated in y-direction and projected on to the $x - z$ plane. Additionally, in this figure, the percentages of absorbed power at each layer are also shown. These percentages show the absorptance of laser within the skin layers, so the rest of
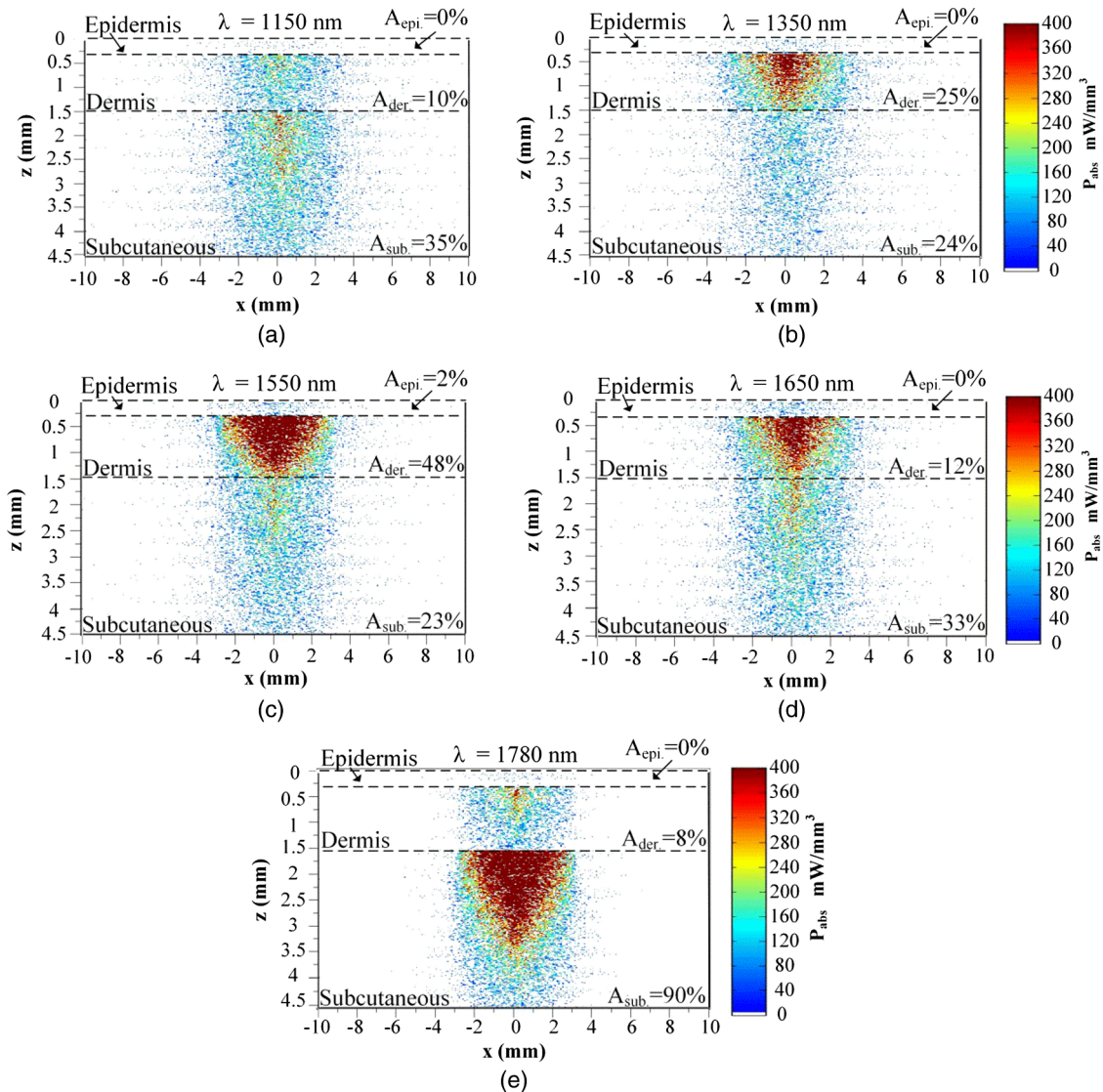

Fig. 4 Location and volumetric density of absorbed power for $P_{in} = 155$ MW at wavelengths of (a) 1150 nm, (b) 1350 nm, (c) 1550 nm, (d) 1650 nm, and (e) 1789 nm. Absorption of each layer is stated in the figure in percentages; x describes the location on x, z represents the distance from the surface, and the colors indicate the volumetric density of absorbed power within the skin.

the energy packets can be either transmitted or backscattered from the skin surface. These results indicate that although the total absorptance of skin is similar at 1150, 1350, and 1650 nm, the spatial distribution of absorbed power within the different layers of skin is quite different. Particularly at 1350 nm, the incident laser power is mostly delivered to the dermis, 25%, whereas in the cases of 1150 and 1650 nm, the subcutaneous layer absorbed the highest percentage of the incident laser power, ~35%. Moreover, the color plots show that the distribution of absorbed power within the skin layers was highly dependent on the wavelength. For example, the volumetric power density was fairly uniform across the dermis and the subcutaneous layer at 1150 nm, whereas high volumetric absorption densities were observed in the dermis at wavelengths of 1350, 1550, and 1650 nm. Furthermore, Fig. 4(e) shows that unlike at any other wavelength considered, power at 1780 nm could penetrate through the epidermis and the dermis and get absorbed by the subcutaneous layer. At this wavelength, 90% of the laser power was absorbed by the subcutaneous layer without significant absorption in the epidermis and the dermis.

3.2 Dosage Delivery at Different Wavelengths

In therapeutic applications, other than the total fraction of power deposited in a particular skin layer, it is also very important to know the volume of tissue subjected to a particular dosage. In order to understand this at the selected wavelengths of this study, Fig. 5 shows the volumes of the dermis and the subcutaneous layers that absorb power densities more than (or equal to) the corresponding amount on x axis. The figure indicates that the volume of treated skin tissue above a given dosage does not necessari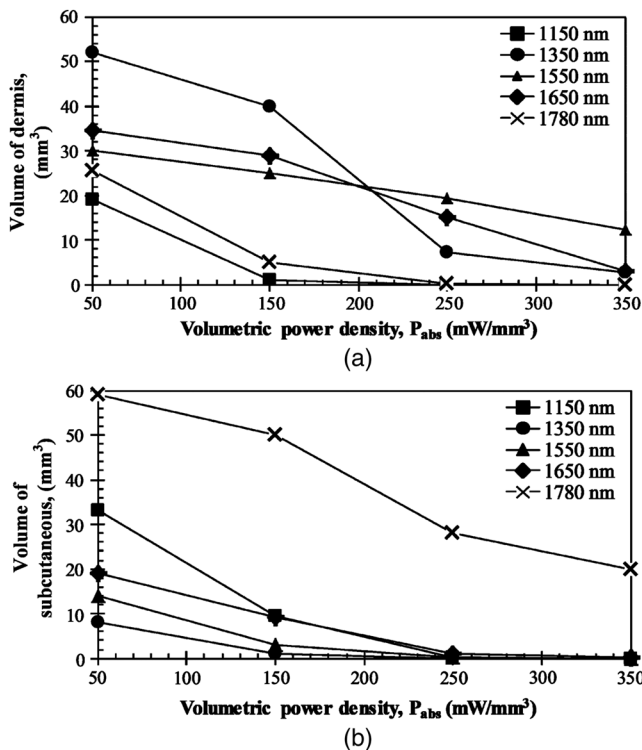ly follow the trends of total fraction of absorbed energy presented in Fig. 4. For example, despite the fact that largest fraction of incident power in the dermis takes place at 1550 nm, as shown in Fig. 4(c), Fig. 5(a) shows that largest volume of the dermis receiving at least 150 mW/mm³ corresponds to 1350 nm. This means that if the dosage necessary for a particular treatment is ~150 mW/mm³ in the dermis, a wavelength of 1350 nm can provide a larger volume of treatment compared to other wavelengths. On the other hand, Fig. 5(b) shows that 1780 nm featured the largest volume of tissue treated in the subcutaneous layer. Particularly, at this wavelength, the volume of the treated subcutaneous layer was ~21 mm³ with power densities exceeding 350 mW/mm³. In this layer, no appreciable volume of tissue received power densities >250 mW/mm³ for all other wavelengths considered.

In order to improve the healing of deep tissue, such as muscle that lies beneath the subcutaneous layer, deep penetration of the laser through the skin is needed.[39,40] In this type of treatment, the total power transmitted through the skin is of interest rather than the local absorptance within the different skin layers. Figure 6 shows the total transmitted power as a function of transport optical thickness based on the simulation results in the considered spectral range. This figure indicates that the transmitted power decreases exponentially with the transport optical thickness. Having similar transport optical thicknesses indicates that the same percentage of incident power will be transmitted through the entire skin, which can be used as a first-order tool for identifying and selecting wavelengths and power for deep tissue LLLT applications. As an example, at a wavelength of 1650 nm, which has the transport optical thickness of 5.5, >41% of the laser power can be delivered to deep tissue, whereas at 1250, 1580, and 1700 nm, with optical thicknesses of 5.6, 5.8, and 8.4, this transmitted power decreases to 37, 29, and 1%, respectively.

3.3 Effect of Spatial Beam Profile on Laser Penetration and Absorption

For many medical laser applications, the beam profile is a critical parameter. It can affect the volumetric dosage as well as the penetration depth of the incident laser power. In the previous analysis, a uniform beam profile was investigated, but a Gaussian profile is often encountered in medical applications.[41] For a laser with a Gaussian profile, the irradiance distribution is given as

Fig. 5 The volume of (a) dermis and (b) subcutaneous that receive power density of at least the indicated amount on the x axis.
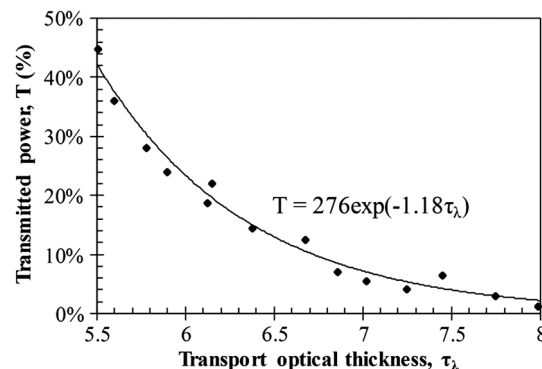

Fig. 6 Correlation between transport optical thickness and the percentage of power that was transmitted through the entire skin without being absorbed.

$$G_{\lambda,xy} = G_{\lambda,\max} \exp\left(-\frac{x^2 + y^2}{\sigma^2}\right), \qquad (11)$$

where $G_{\lambda,xy}$ is the local irradiance and $G_{\lambda,\max}$ is the irradiance at the beam center ($x = 0$, $y = 0$). σ is the divergence radius, which indicates the specific annular distance from the center, where $1/e$ of maximum irradiance has been reached. By varying this parameter, the laser beam profile can be changed from a very sharp peak when $\sigma \to 0$ to the uniform profile at $\sigma \to \infty$. In order to understand the effect of different spatial beam profiles on penetration and absorption, three Gaussian beam profiles have been considered. The total power of the beams considered here was the same in all cases, but each featured a different divergence radius within the practical range from 0.1 to 10 mm.[41] Thus, divergence radii of 1, 2, and 10 mm were selected for these Gaussian profiles. We simulated the propagation of these beams at the wavelength of 1350 nm in skin and compared the results with those of the uniform profile case. Although the total absorbed and transmitted power through the entire skin was similar, there was a significant difference in the local volumetric dosages. Figure 7 shows the volumetric dosage for different beam profiles at the wavelength of 1350 nm. According to this figure, for the Gaussian beam with divergence radii of 10 mm, the distribution of absorbed power was similar to that of a uniform beam profile. However, smaller divergence radii result in highly localized larger volumetric dosages along the centerline of the beam.

To further illustrate this point, Fig. 8 shows the volumetric dosage at the two different locations with respect to the beam center, namely at the beam center, $x = 0$ mm, and 2 mm away from the beam center, $x = \pm 2$ mm. Figure 8(a) shows that by
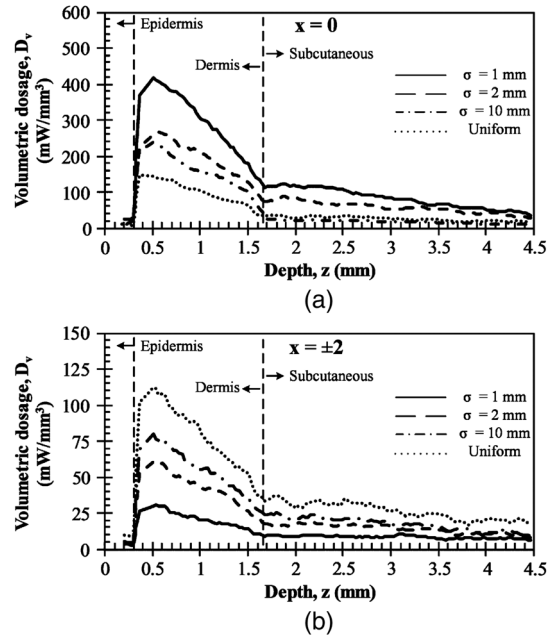

Fig. 8 The volumetric dosage versus depth from the surface for $P_{in} = 155$ mW, at two locations of (a) $x = 0$ and (b) $x = 2$ mm; x is the distance from the center of the beam.

changing the beam profile from uniform to Gaussian, the dosage of absorbed power can be increased from 150 to 450 mW/mm³ in the dermis along the beam center. Similarly, in the subcutaneous layer, the local dosage was about three times higher for the sharpest Gaussian profile in comparison to a uniform beam. However, according to Fig. 8(b), at $x = \pm 2$ mm, the local
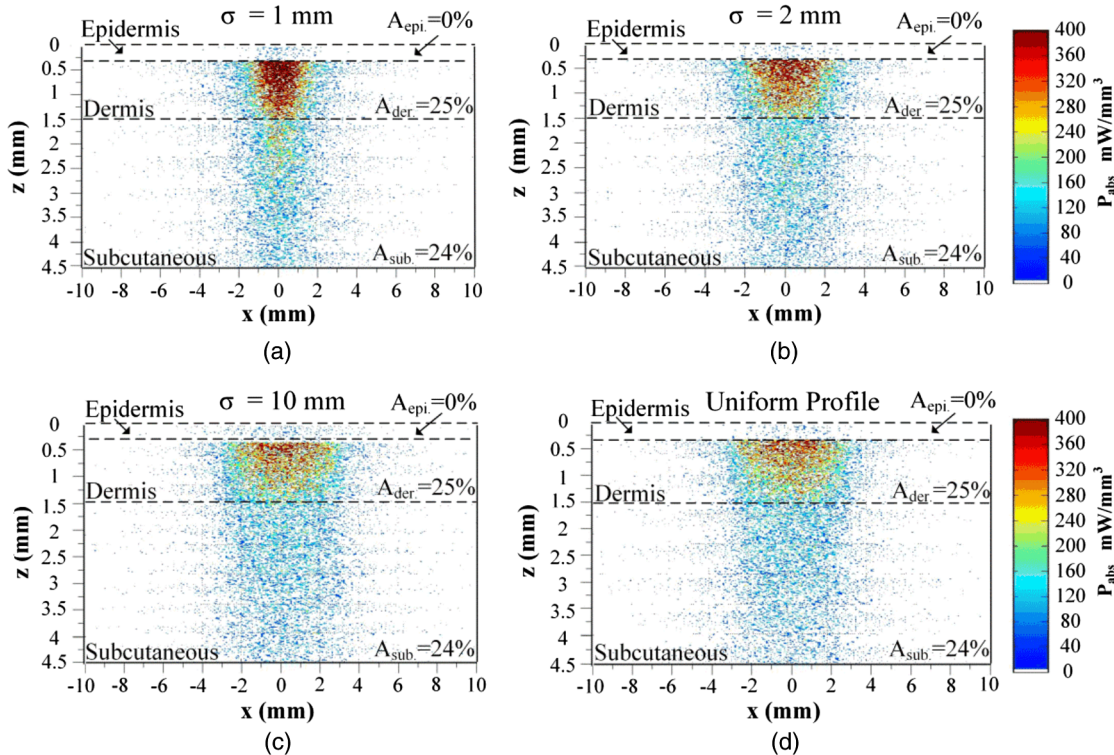

Fig. 7 Location and volumetric dosage of absorbed energy for $P_{in} = 155$ mW and $t = 10$ s, at the wavelength of 1350 nm, for Gaussian beam profiles with divergence radii of (a) 1 mm, (b) 2 mm, (c) 10 mm, and (d) uniform beam profile.

Table 2 Maximum permissible exposure duration for the wavelengths of 1150, 1350, 1550, 1650, and 1780 nm at the power of p_{laser} (mW) according to ANSI Z136.1-2007.[39]

Wavelength (nm)	Permissible power range (mW)	Maximum permissible exposure duration (s)
1150	$p_{laser} \leq 10^3$	$2.9/p_{laser}$
1350	$p_{laser} \leq 10^3$	$2.3/p_{laser}$
1550	$p_{laser} \leq 700$	$10/p_{laser}$
1650	$p_{laser} \leq 700$	$10/p_{laser}$
1780	$p_{laser} \leq 700$	$10/p_{laser}$

dosage in the dermis and the subcutaneous layer decreased from 120 to 40 mW/mm^3 and from 30 to 10 mW/mm^3, respectively.

3.4 Exposure Duration and Skin Damage

Skin damage threshold can be defined as a critical amount of absorbed radiation energy which causes permanent denaturation of skin cells. Above a critical dosage, laser irradiation causes necrosis of tissue cells and lethal damage to superficial blood vessels.[42,43] In order to prevent this damage, the American National Standards Institute (ANSI) provides the maximum permissible exposure (MPE) per area as a function of duration of exposure for different wavelengths based on experimental results.[44] These MPE data include the visible and NIR part of the electromagnetic spectrum for wavelengths from 400 to 2600 nm. To find the MPE duration of the studied wavelengths, we obtained the maximum absorbed fluence within the skin (i.e., absorbed power per area) from our simulations and applied the ANSI specifications at the corresponding wavelengths. Table 2 shows the MPE duration at the considered wavelengths with the laser power of p_{laser} expressed in milliwatts. In this table, the beam diameter was considered to be 6.1 mm; however, a sensitivity analysis was performed to ensure that the beam diameter does not affect the MPE values by >2% in the diameter range from 5 to 15 mm.

Thus, the maximum exposure durations can easily be calculated using Table 1 for lasers with typical powers within the ranges of LLLT. For example, for the studied laser (i.e., 155 mW), the maximum exposure durations for the wavelengths of 1150 and 1350 nm are ~19 and 15 s, respectively. In addition, for higher wavelengths of 1550, 1650, and 1780 nm, this duration can be increased up to 64 s.

4 Conclusion

This paper presented a numerical study on the penetration and the absorption of laser beams of different spatial profiles through a three-layer human skin model over the spectral range from 1000 to 1900 nm. Based on the results obtained, it was shown that the choice of wavelength and the beam profile significantly affect the spatial distribution, volumetric dosage, and magnitude of absorbed power density and enable targeted treatment of different skin layers. It was shown that by changing the laser wavelength from 1550 to 1780 nm, the absorption in the subcutaneous layer can be increased by 67%; however, the absorption in the dermis will be decreased by 40%. Moreover, it was demonstrated that transport optical thickness

can be used as a first-order indicator for determining the relative penetration depths of different wavelengths in skin. In addition, maximum exposure durations for the considered wavelengths were discussed based on the ANSI standards. Finally, the results presented are expected to provide LLLT technology developers insight and guidance on wavelength, dosage, beam profile, and power selection.

References

1. Y.-Y. Huang et al., "Biphasic dose response in low level light therapy," *Dose-Response* **7**(4), 358–383 (2009).
2. L. I. Fillipin et al., "Low-level laser therapy (LLLT) prevents oxidative stress and reduces fibrosis in rat traumatized achilles tendon," *Laser Surg. Med.* **37**(4), 293–300 (2005).
3. C. F. Rizzi et al., "Effects of low-level laser therapy (LLLT) on the nuclear factor (NF)-kB signaling pathway in traumatized muscle," *Laser Surg. Med.* **38**(7), 704–713 (2006).
4. J. T. Hopkins et al., "Low-level laser therapy facilitates superficial wound healing in humans: a triple-blind, sham-controlled study," *J. Athl. Train.* **39**(3), 223–229 (2004).
5. W. Poseteb et al., "Low-level laser therapy for wound healing: mechanism and efficacy," *Dermatol. Surg.* **31**(3), 334–340 (2005).
6. L. Almeida-Lopez et al., "Comparison of the low level laser therapy effects on cultured human gingival fibroblasts proliferation using different irradiance and same fluence," *Laser Surg. Med.* **29**(2), 179–184 (2001).
7. R. P. Abergel, E. Glassberg, and J. Uitto, "Increased wound-healing rate in pig skin treated by helium-neon laser," *Proc. SPIE* **0908**, 6–11 (1988).
8. J. M. Bjordal et al., "Low-level laser therapy in acute pain: a systematic review of possible mechanisms of action and clinical effects in randomized placebo-controlled trials," *Photomed. Laser Surg.* **24**(2), 158–168 (2006).
9. A. N. Bashkatov, E. A. Genina, and V. V. Tuchin, "Optical properties of skin, subcutaneous, and muscle tissues: a review," *J. Innov. Opt. Health Sci.* **4**(1), 9–38 (2011).
10. A. S. da Rosa et al., "Effects of low-level laser therapy at wavelengths of 660 and 808 nm in experimental model of osteoarthritis," *Photochem. Photobiol.* **88**(1), 161–166 (2012).
11. J. Taradaj et al., "Failure of low-level laser therapy to boost healing of venous leg ulcers in surgically and conservatively treated patients," *Phlebologie* **37**(5), 227–282 (2008).
12. S. L. Jacques and M. Keijzer, "Dosimetry for lasers and light in dermatology: Monte Carlo simulation of 577-nm pulsed laser penetration into cutaneous vessels," *Proc. SPIE* **1422**, 2–13 (1991).
13. M. J. C. van Gemert et al., "Wavelengths for port wine stain laser treatment: influence of vessel radius and skin anatomy," *Phys. Med. Biol.* **42**(1), 41–50 (1997).
14. B. Choi, B. Majaron, and J. S. Nelson, "Computational model to evaluate port wine stain depth profiling using pulsed photothermal radiometry," *J. Biomed. Opt.* **9**(2), 299–307 (2004).
15. W. C. Y. Lo and L. Lilge, "Accelerated 3-D Monte Carlo light dosimetry using a graphics processing unit (GPU) cluster," *Proc. SPIE* **7376**, 737609 (2010).
16. L. Wang, S. L. Jacques, and L. Zheng, "MCML—Monte Carlo modeling of light transport in multi-layered tissues," *Comput. Methods Programs Biomed.* **47**(2), 131–146 (1995).
17. S. Prahl et al., "A Monte Carlo model of light propagation in tissue," *Proc. SPIE* **IS 5**, 102–111 (1989).
18. T. Roeva, T. Petrov, and N. Minkovsky, "Results of the trials and light delivery evaluation at low level laser therapy of acute and chronic pain," *Proc. SPIE* **5449**, 489–493 (2004).
19. E. Stoykova and O. Sabotinov, "Precise optical dosimetry in low level laser therapy of soft tissues in oral cavity," *Proc. SPIE* **5449**, 474 (2004).
20. P. Parvin, S. Eftekharnoori, and H. R. Dehghanpour, "Monte Carlo simulation of photon densities inside the dermis in LLLT (low level laser therapy)," *Opt. Spectrosc.* **107**(3), 486–490 (2009).

21. J. Bensouilah et al., *Aromadermatology: Aromatherapy in the Treatment and Care of Common Skin Conditions*, Radcliffe Publishing, Abington (2006).

22. R. Marchesini et al., "Extinction and absorption coefficients and scattering phase functions of human in vitro," *Appl. Opt.* **28**(12), 2318–2324 (1989).

23. C. R. Simpson et al., "Near-infrared optical properties of ex vivo human skin and subcutaneous tissues measured using the Monte Carlo inversion technique," *Phys. Med. Biol.* **43**(9), 2465–2478 (1998).

24. M. F. Modest, *Radiative Heat Transfer*, Academic Press, New York (2003).

25. T. L. Troy and S. N. Thennadil, "Optical properties of human skin in the near infrared wavelength range of 1000 to 2200 nm," *J. Biomed. Opt.* **6**(2), 167–176 (2001).

26. I. V. Meglinski and S. J. Matcher, "Quantitative assessment of skin layers absorption and skin reflectance spectra simulation in the visible and near-infrared spectral regions," *Physiol. Meas.* **23**(4), 741–753 (2002).

27. K. Iino et al., "Monte Carlo simulation of near infrared reflectance spectroscopy in the wavelength range from 1000 nm to 1900 nm," *Opt. Rev.* **10**(6), 600–606 (2003).

28. E. Salomatina et al., "Optical properties of normal and cancerous human skin in the visible and near-infrared spectral range," *J. Biomed. Opt.* **11**(6), 064026 (2006).

29. D. Zhu et al., "Effect of light losses of sample between two integrating spheres on optical properties estimation," *J. Biomed. Opt.* **12**(6), 064004 (2007).

30. W. G. Zijlstra, A. Buursma, and W. P. M. der Roest, "Absorption spectra of human fetal and adult oxyhemoglobin, de-oxyhemoglobin, carboxyhemoglobin, and methomoglobin," *Clin. Chem.* **37**(9), 1633–1638 (1991).

31. T. Wissel et al., "Estimating soft tissue thickness from light-tissue interactions—a simulation study," *Biomed. Opt. Express* **4**(7), 1176–1187 (2013).

32. E. Alerstam, T. Svensson, and S. Andersson-Engels, "Parallel computing with graphics processing units for high-speed Monte Carlo simulation of photon migration," *J. Biomed. Opt.* **13**(6), 060504 (2008).

33. Y. Fukui, Y. Ajichi, and E. Okada, "Monte Carlo prediction of near-infrared light propagation in realistic adult and neonatal head models," *Appl. Opt.* **42**(16), 2881–2887 (2003).

34. D. Y. Churmakov et al., "Analysis of skin tissues spatial fluorescence distribution by the M\onte Carlo simulation," *J. Phys. D: Appl. Phys.* **36**(14), 1722–1728 (2003).

35. N. Metropolis and S. Ulam, "The Monte Carlo method," *JASA* **44**(247), 335–341 (1949).

36. H. Kahn and T. E. Harris, "Estimation of particle transmission by random sampling Monte Carlo method," *Nat. Bur. Std. Appl. Math.* **12**, 27–30 (1951).

37. D. M. Wieliczka, S. Weng, and M. R. Querry, "Wedge shaped cell for highly absorbent liquids: infrared optical constants of water," *Appl. Opt.* **28**(9), 1714–1719 (1989).

38. H. C. van de Hulst, *Multiple Light Scattering*, Academic Press, New York (1980).

39. M. R. Hamblin and T. N. Demidova, "Mechanisms of low level light therapy," *Proc. SPIE* **6140**, 614001 (2006).

40. L. Zhao et al., "Effect of different LLLT on pituitrin-induced bradycardia in the rabbit," *Laser Med. Sci.* **21**(2), 61–66 (2006).

41. S. Saghafi et al., "Effects of laser beam shapes on depth of penetration in dermatology," *Proc. SPIE* **6191**, 619107 (2006).

42. B. Chen, R. J. Thomas, and A. J. Welch, "Modeling thermal damage in skin from 2000-nm laser irradiation," *J. Biomed. Opt.* **11**(6), 064028 (2006).

43. C. P. Chain et al., "Porcine skin visible lesion thresholds for near-infrared lasers including modeling at two pulse durations and spot sizes," *J. Biomed. Opt.* **11**(4), 041109 (2006).

44. American National Standards Institute Inc., *American National Standard for Safe Use of Lasers*, Laser Institute of America, Orlando (2007).

Babak Nasouri earned his bachelor's degree from Sharif University of Technology, Tehran/Iran in July 2012. He earned his MS degree in mechanical engineering department at The University of Texas at Austin in May 2014. His MS thesis was on simulating light penetration in tissue, using forward and inverse Monte Carlo methods. He is now a PhD student in mechanical engineering department of University of British Columbia in Vancouver, Canada.

Thomas E. Murphy earned his BS with honors in mechanical engineering from Brown University in 2009. He earned his PhD in mechanical engineering at the University of Texas at Austin in 2013. His dissertation was on the design and operation of a synthetic tree for water and energy efficient algae cultivation. He is now a postdoctoral researcher at NASA Ames Research Center, where he studies interactions between light and photosynthetic organisms in microbial mat communities.

Halil Berberoglu is an assistant professor at mechanical engineering department and he is a member of the Institute for Cell and Molecular Biology at the University of Texas at Austin. His research integrates transport phenomena, thermodynamics, and interfacial science with microbiology and systems analysis, for applications in energy systems, biotechnology, and manufacturing.